(This is a sample cover image for this issue. The actual cover is not yet available at this time.)

Remote Sensing of Environment 131 (2013) 182–194

Contents lists available at SciVerse ScienceDirect

Remote Sensing of Environment

journal homepage: www.elsevier.com/locate/rse

Recovering missing pixels for Landsat ETM + SLC-off imagery using multi-temporal regression analysis and a regularization method

Chao Zeng [a], Huanfeng Shen [b,*], Liangpei Zhang [a,*]

[a] The State Key Laboratory of Information Engineering in Surveying, Mapping and Remote Sensing, Wuhan University, Wuhan, Hubei, 430079, China
[b] School of Resource and Environmental Science, Wuhan University, Wuhan, Hubei, 430079, China

ARTICLE INFO

Article history:
Received 7 September 2012
Received in revised form 13 December 2012
Accepted 14 December 2012
Available online xxxx

Keywords:
ETM+
SLC-off
Gap filling

ABSTRACT

Since the scan line corrector (SLC) of the Landsat Enhanced Thematic Mapper Plus (ETM+) sensor failed permanently in 2003, about 22% of the pixels in an SLC-off image are not scanned. To improve the usability of the ETM+ SLC-off data, we propose an integrated method to recover the missing pixels. The majority of the degraded pixels are filled using multi-temporal images as referable information by building a regression model between the corresponding pixels. When the auxiliary multi-temporal data cannot completely recover the missing pixels, a non-reference regularization algorithm is used to implement the pixel filling. To assess the efficacy of the proposed method, simulated and actual SLC-off ETM+ images were tested. The quantitative evaluations suggest that the proposed method can predict the missing values very accurately. The method performs especially well in edges, and is able to keep the shape of ground features. According to the assessment results of the land-cover classification and NDVI, the recovered data are also suitable for use in further remote sensing applications.

1. Introduction

From the first Landsat satellite launched in 1972 to the present, the Landsat satellite series has provided the longest continuous multispectral terrestrial observation program (Arvidson et al., 2006; Lauer et al., 1997; Lee et al., 2004). Due to the relatively high spatial resolution, the Landsat data are informative with regard to human activities on Earth's surface. Furthermore, the opening of the entire United States Geological Survey (USGS) Landsat archive has made all of the USGS Landsat imagery freely available through a web portal (http://glovis.usgs.gov/) (Woodcock et al., 2008). This has resulted in an increased capacity to undertake ambitious analyses of terrestrial dynamics across large areas, using a dense time series of imagery. These benefits have made Landsat imagery an invaluable information source to both scientists and policy makers. Landsat-7, which carries the Enhanced Thematic Mapper Plus (ETM+) sensor, is the latest version of the Landsat series. It was launched in April 1999 and has sufficient fuel to maintain operations through to 2016 (Wulder et al., 2011). The spatial resolution of the ETM+ multispectral bands is 30 m, and the swath is 185 km. The ETM+ sensor has a narrow 15° field of view and overpasses every location on Earth every 16 days (Lee et al., 2004; Markham et al., 2006). Because of its excellent image quality, Landsat-7 data have been widely used in agriculture, geological surveys, global change detection, mapping, archeology, and planning management.

On May 31, 2003, the scan line corrector (SLC) of the ETM+ sensor on board Landsat-7 failed permanently. The SLC is an electromechanical device that compensates for the forward motion of the satellite within the ETM+ scanning. When operating properly, it ensures that the sensor's forward and reverse cross-track scanning pattern provides a continuous coverage of the full Landsat swath. With a non-functioning SLC, instead of aligning in parallel scans, the individual scans alternately overlap and leave large wedge-shaped gaps that range from a single pixel in width near the image nadir to about 14 pixels width towards the edges of the scene (USGS, 2003). Only in the center of the image (approximately 22 km wide) do the scans give near-contiguous coverage of the surface scanned below the satellite. To differentiate the degraded data, the images acquired before the SLC failure are designated as 'SLC-on' images, and those acquired after the SLC failure are designated as 'SLC-off' images. Approximately 22% of the SLC-off image data are lost, and these parts are filled with zero values in the commonly used L1G products (radiometrically and geometrically corrected, rotated and georeferenced) (Arvidson et al., 2006; Ju & Roy, 2008; Wulder et al., 2011).

Although the anomalous Landsat-7 data resulting from the SLC failure have become a major obstacle for Landsat ETM+ data applications, some users still prefer these data over more costly alternatives (USGS, 2003). Moreover, with the failure of Landsat-5, SLC-off ETM+ data are the only Landsat data currently being acquired for related applications. Consequently, the SLC-off data have become particularly important for applications using a long time series of Landsat imagery. The gap-filling in SLC-off ETM+ images is therefore necessary to ensure the continuity of this longest satellite observation series. However, it

* Corresponding authors. Tel.: +86 13163235536.
E-mail addresses: shenhf@whu.edu.cn (H. Shen), zlp62@public.wh.hb.cn (L. Zhang).

0034-4257/$ – see front matter © 2013 Elsevier Inc. All rights reserved.
http://dx.doi.org/10.1016/j.rse.2012.12.012

has been found that new tools and techniques to compensate for the missing information can improve the usability of the deteriorated images, and a number of interesting approaches have been developed. These approaches can be divided into three types: one type is the non-reference methods, which fill the gaps directly, without any additional references; the second type uses multi-temporal Landsat data to fill the black strips by predicting the un-scanned values; and the last type of method exploits auxiliary data from other sensors to recover the missing information.

The non-reference recovery approaches usually employ resampling algorithms. The most commonly used resampling algorithms include nearest neighbor, bilinear, and cubic convolution. Only a few of these approaches utilize the spatial information, and these simple interpolation methods are not appropriate for ETM+ image recovery. Zhang et al. (2007) proposed using the kriging geostatistical technique to fill the data gaps. This case study showed that the ordinary kriging techniques can provide a useful tool for interpolating the missing pixels. However, the intrinsic stationarity assumption, a theoretical premise of the geostatistical methods, is not always valid, especially for heterogeneous landscapes (Pringle et al., 2009; Van der Meer, 2012).

Compared with the non-reference methods, the approaches using auxiliary data are much more attractive. It is evident that the most convenient auxiliary data are the multi-temporal Landsat images. Therefore, methods using multiple Landsat images have been widely developed. Soon after SLC-off occurred, a report compiled by the USGS Earth Resources Observation and Science Center (EROS) suggested that the un-scanned gaps could be compensated for by previous SLC-on images of the same area (Storey et al., 2005). A simple local histogram matching method was adopted in this early phase. As the gap-covered locations vary in the different scenes, this allows the possibility of restoring the missing pixels with multi-temporal SLC-off data. An improved method using multiple SLC-off images was subsequently developed by the EDC, where every missing value is obtained by employing a local linear histogram matching in a moving window. This method is very simple and easy to implement, and can perform well in most regions if the input scenes are of high quality. Nevertheless, it tends to be more sensitive with regard to data selection and has difficulty with heterogeneous landscapes where the features are smaller than the local moving window size (USGS, 2003). As an alternative, Maxwell et al. (2007) developed another approach which uses a multi-scale segment model derived from a previous SLC-on image to guide the spectral interpolation across the gaps. However, this method has the disadvantage of having lower accuracy at the pixel level, especially for narrow features such as roads and streams (Maxwell et al., 2007). Boloorani et al. (2008a) developed a projection transformation method to fill the gaps. Unlike the other methods, absolute radiometric correction is a vital preprocessing step for this algorithm. In addition, SLC-on imagery acquired before 2003 is unreliable if landscape structural changes have occurred. A geostatistics-based method using multi-temporal SLC-off images has also been developed, in which co-kriging techniques are used to recover the invalid pixels (Pringle et al., 2009). Although this study showed that geostatistical methods can be effective, accurate prediction is still difficult at the junction of different land-use types (Pringle et al., 2009). Chen et al. (2011) developed a method known as the neighborhood similar pixel interpolator (NSPI), and it was found that NSPI can restore the value of un-scanned pixels accurately, even in heterogeneous regions.

Approaches using data from other sensors have also been developed. Boloorani et al. (2008b) proposed to use the information observed by the Advanced Land Imager (ALI) on board the Earth Observing One (EO-1) satellite, while Roy et al. (2008) chose MODIS imagery as a source of complementary information. Reza and Ali (2008) used IRS products to recover the defective images. Chen et al. (2010) estimated the value of un-scanned pixels using auxiliary data from the China–Brazil Earth Resources Satellite-02B (CBERS-02B). Although these methods can effectively compensate for the missing information, using information from non-Landsat sensors has the disadvantages of the issues of spectral compatibility, spatial resolution and financial constraints.

Since the development of the above methods, the usability of ETM+ images has been greatly improved. However, these methods all have their respective advantages and limitations. Generally, the methods based on multi-temporal images are more attractive, but the missing pixels can often not be filled completely, due to the lack of appropriate auxiliary images. In this paper, a recovery method integrating the advantages of a multi-temporal approach and a non-reference approach is proposed. With the complementary information from multi-temporal SLC-off images, a weighted linear regression (WLR) algorithm is proposed to recover the missing pixels accurately in complex landscape areas. Furthermore, a regularization algorithm is presented to fill the possible remaining gaps which could not be covered by the auxiliary multi-temporal images.

2. Methodology

For convenience, in this paper, an SLC-off image to be restored is defined as the primary image, while an auxiliary image is referred to as the fill image. An un-scanned pixel in the gaps of the primary image is defined as a target pixel, and the respective location is named the target location. Two types of recovery method are presented in this paper: when there are multi-temporal images as the input, WLR is implemented to fill in the missing pixels in the primary image; if there are no auxiliary images, or the auxiliary images do not contain sufficient complementary information (i.e. the gaps cannot be completely covered by valid pixels), a non-reference regularization recovery method is provided to fill the remaining missing pixels.

2.1. The weighted linear regression based multi-temporal recovery method

It is noteworthy that, even for data acquired from the same sensor, the reflectance of the same location may be different in multi-temporal images. These differences can be divided into three kinds: one kind of difference is due to the effects of the variation in the observation conditions; another comes from the regular changes in the objects; and the third kind of difference is caused by an abrupt transformation in the target type. Generally, the first kind of difference has less impact on the imaging process and can allow a better correction than the other two kinds. The second kind of difference can be widely found over most scenes, for example as seasonal vegetation change. If the change is regular, the tendency can be predicted by auxiliary information. The third kind of difference is usually related to human activities such as urban expansion. This brings about significant spectral change, which can be very difficult to predict. Conventionally, to minimize the error brought about by this kind of change, it is necessary to choose scenes that are as close in time to the primary scene as possible. As abrupt scene changes are unpredictable, like most studies, we do not discuss this issue in the recovery approach.

In the early studies, a linear relationship was often assumed between multi-temporal scenes (Storey et al., 2005; USGS, 2003). As an example, a simple analysis using two ETM+ images is presented here. The 400×400 pixels Landsat area is located at Jilin, China, around 42.62°N and 127.17°E. Fig. 1(a) and (b) shows the SLC-on ETM+ images acquired on May 28, 2002, and April 26, 2002, respectively. The red bands (band 3) of the two images are shown in Fig. 1(c) and (d), and a classified scatterplot is shown in Fig. 1(e). The location of the classes is shown in Fig. 1(f). The basically unchanged water and building regions are classified as yellow in the scatterplot. The vegetation and arable land areas are marked as green and red, respectively. The corresponding regions show different changes. Generally, according to the scatterplot, the relationships between the two images cannot be uniformly described. However, there are obvious linear relationships for the pixels belonging to similar ground features.

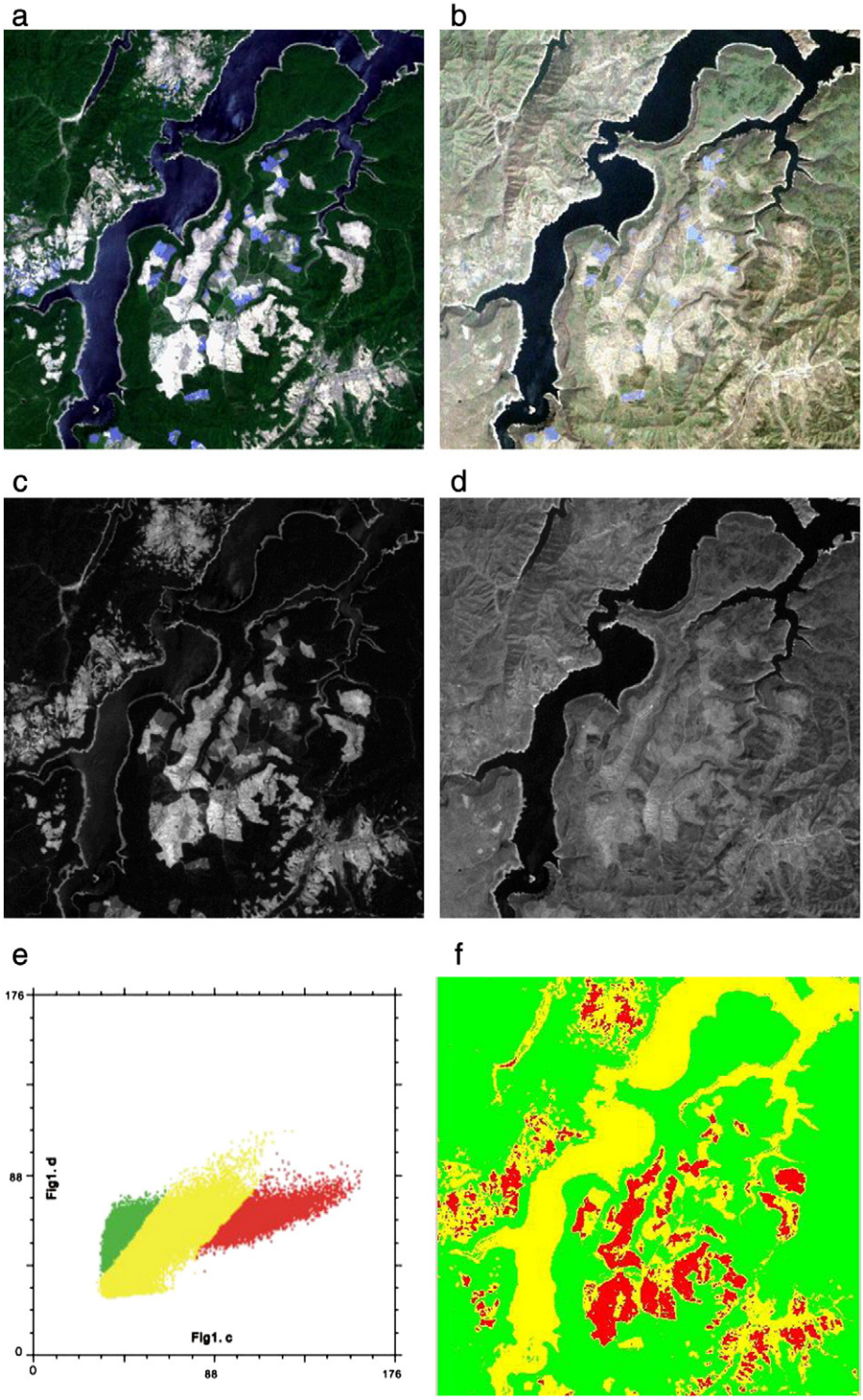

Fig. 1. Landsat ETM+ images for the case study area: (a)–(b) ETM+ image acquired on May 28, 2002, and April 26, 2002, respectively; (c)–(d) the corresponding band 3 images of (a) and (b); (e) the scatterplot of (c) versus (d), classified as red = arable land, green = vegetation, and yellow = water/urban; (f) location map of the marked points in (e). (For interpretation of the references to color in this figure legend, the reader is referred to the web version of this article.)

We propose that every single missing pixel can be recovered using a linear relationship calculated from locally similar pixels. Then, the hypothesis can be represented as:

$$p_t = a \cdot f_t + b \tag{1}$$

where p_t and f_t are the pixels at the target location (t) in the primary image and fill image, respectively, and a and b are regression coefficients calculated from the locally similar pixels. Accordingly, we must first select the similar pixels of the target location in the primary and fill images. Considering that the spectral values in each band can vary greatly, it is unreasonable to determine the spectral similarity by

a fixed qualification. In this study, an adaptive determination procedure for the similar pixels is proposed. For each target pixel in each band, the *i*th similar pixel must meet the following equation:

$$|f_i - f_t| \le T \tag{2}$$

where f_i and f_t are the values of the similar pixel and target pixel in the fill image, and T is the adaptive threshold, calculated pixel by pixel and band by band. Here, the threshold is determined by the local standard variation:

$$T = \sqrt{\sum_{i=1}^{n} (f_i - \mu)^2}, \tag{3}$$

where μ is the mean value of a local area. In this paper, the size of this area is empirically set as a 5-pixel by 5-pixel window. Therefore, the value of T represents the smoothness of the local area. The requirements of Eqs. (2) and (3) ensure that the appropriate similar pixels can be selected in the various regions.

After the determination of T, similar pixels are then selected according to Eqs. (2) and (3) in a search window. The common valid pixels of the primary and fill images that are located in this window are all involved. For each target pixel, an adaptive window is used for the similar pixel searching. To guarantee the robustness of the follow-up regression algorithm, the reference value of the number of selected similar pixels is set as N_R. The window size is first set at an initial value. If the number of selected similar pixels cannot meet the reference value N_R, the window size will be enlarged by two pixels. Considering that too large a window will take a lot of computing time, a maximum window size can be set. Essentially, the initial window size and the maximum window size are both largely affected by N_R. The determination of these parameters will be discussed in Section 3.

The coefficients can then be calculated from the selected pixels (Eq. 1). One of the most commonly used methods is least-squares estimation. However, it is clear that the contributions of each pixel vary due to the spectral and spatial differences. In our method, a higher spectral similarity and a smaller distance for a similar pixel to the target pixel is assigned a larger weight. Combining the spectral and spatial differences, a synthetic difference index can be computed as:

$$D_i = |f_i - f_t + \alpha| \cdot \left((x_i - x_t)^2 + (y_i - y_t)^2 \right), \tag{4}$$

where x_i, y_i, x_t and y_t represent the locations of the similar pixel and target pixel, and α is a small value to prevent D_i equaling zero. The term $((x_i - x_t)^2 + (y_i - y_t)^2)$ describes the spatial difference between the corresponding similar pixel and the target pixel in the fill image, and $|f_i - f_t + \alpha|$ represents the spectral difference. It should be noted that if the spectral value of the similar pixel equals the value of the target pixel, D_i will be 0 without α. However, it is unreasonable to deem that there is no difference between the two pixels. Therefore, we set a small value of α to avoid this condition.

The weights of each selected similar pixel are then normalized as:

$$W_i = (1/D_i) / \sum_{i=1}^{N} (1/D_i). \tag{5}$$

After normalization, the range of weight W_i is from 0 to 1, and the sum of all the selected similar pixel weights is 1.

Subsequently, the WLR algorithm is employed to calculate the coefficients. Generally, the regression equation can be solved by the weighted least-squares method. For convenience, the expanded form is given as (Ruppert & Wand, 1994):

$$a = \frac{\sum_{i=i}^{n} W_i (p_i - \overline{p}) \left(f_i - \overline{f} \right)}{\sum_{i=i}^{n} W_i \left(f_i - \overline{f} \right)^2} \tag{6}$$

and

$$b = \overline{p} - a\overline{f} \tag{7}$$

where $\overline{p}$ and $\overline{f}$ are the mean values of all the similar pixels in the search window on the primary and fill image, respectively.

For particularly small objects, it is possible that only a few, or even no similar pixels will be found in the procedure. In the case that the reference number of similar pixels, N_R, does not meet the set value when the window size reaches the maximum size, but the number is more than 2, the WLR algorithm will still be performed using all the selected similar pixels. For the exceptional situation when there are not enough similar pixels for the algorithm, the target pixel will be identified as an outlier. In this condition, the target pixel value will be adjusted to fit the environment. Therefore, the coefficient is calculated by:

$$a = \frac{\overline{p}}{\overline{f}} \tag{8}$$

and

$$b = 0 \tag{9}$$

where μ_p and μ_f are the mean values of all the common pixels in the window of the primary image and fill image, respectively.

2.2. The regularization based non-reference recovery method

Due to the different degrees of gap overlapping, two or more auxiliary images are needed in a multi-temporal recovery procedure. It is often the case that the available images are not sufficient to fill all the missing pixels because the gaps cannot be completely covered. In this case, it is necessary to recover the remaining pixels using a non-reference recovery method. In this paper, a regularization method is presented for this problem. The recovery framework can be written as:

$$\mathbf{p} = \arg\min[\mathrm{E}(\mathbf{p})], \tag{10}$$

where

$$\mathrm{E}(\mathbf{p}) = ||\mathbf{Q}(\mathbf{p}' - \mathbf{p})||^2 + \lambda \mathbf{R}(\mathbf{p}), \tag{11}$$

is the cost function, in which $\mathbf{p}'$ and $\mathbf{p}$ represent the input primary image and the desired primary image, respectively, $\mathbf{R}(\mathbf{p})$ represents the regularized model, and λ is the regularization parameter. Here, $\mathbf{Q}$ is a diagonal matrix representing the reliable information in the different pixel locations, and its row number equals the image size. For the recovery issue, the element values are set to one for all the valid pixels, and to zero for the missing pixels. As for $\mathbf{R}(\mathbf{p})$, models such as the Laplacian prior, Gauss–Markov prior and total variation prior have been widely used (Shen & Zhang, 2009; Shen et al., 2010; Yuan et al., 2012; Zhang et al., 2011). Generally, the latter two priors give a better performance in edge-preserving but take a longer time (Strong & Chan, 2003). Since the spatial resolution of ETM+ is not very high, there are seldom sharp edges in the image. By further considering the computational efficiency,

the Laplacian model is more appropriate for this work. Therefore, the cost function can be written as:

$$E(\mathbf{p}) = ||\mathbf{Q}(\mathbf{p}'-\mathbf{p})||^2 + \lambda \mathbf{L}\mathbf{p}^2 \quad (12)$$

where **L** is the Laplacian operator. The only parameter requiring predetermination in this method is the regularization parameter λ. According to Eq. (12), the regularization parameter λ balances the data fidelity (the first term) and the image regularization (the second term). In this paper, λ was empirically set as 0.01.

Differentiating E(**p**) with respect to **p** gives:

$$\nabla E(\mathbf{p}) = -2\mathbf{Q}^T\mathbf{Q}(\mathbf{p}'-\mathbf{p}) + 2\lambda \mathbf{L}^T\mathbf{L}\mathbf{p}. \quad (13)$$

Due to the problems involved with finding a solution to an equation like Eq. (13), an iterative method using an initial guess to generate

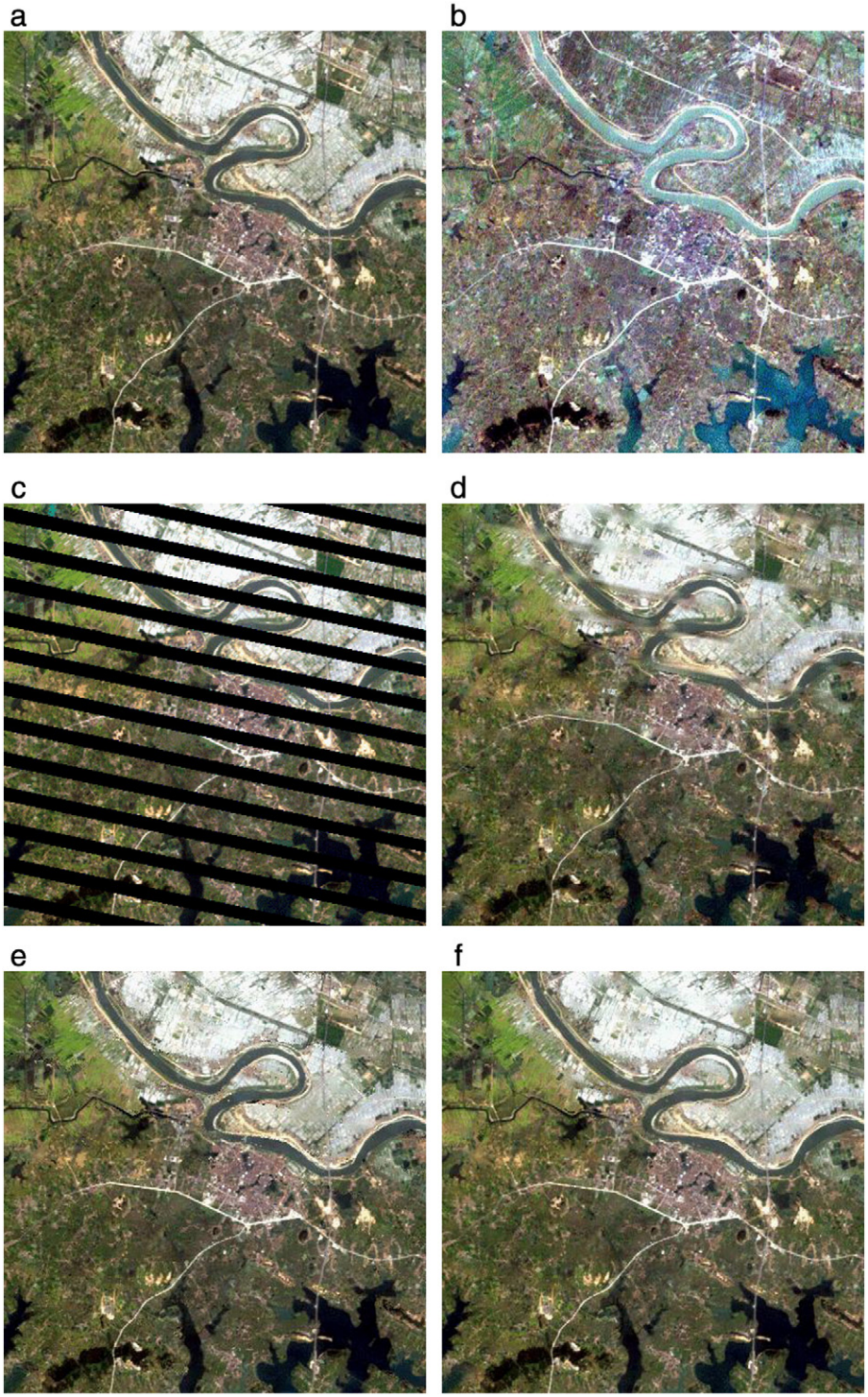

Fig. 2. Landsat SLC-on ETM + images for the simulated experiment: (a)–(b) acquired on March 19, 2002, and December 29, 2001, respectively; (c) SLC-off image simulated by (a); (d), (e) and (f) are the results recovered by LLHM, NSPI and WLR, respectively.

successive approximations to a solution is often adopted. Thus, the desired image can be solved by employing the successive approximations iteration:

$$\hat{\mathbf{p}}_{n+1} = \hat{\mathbf{p}}_n - \beta_n \nabla \mathrm{E}(\mathbf{p}_n) \tag{14}$$

where n is the iteration number, and β_n is the step size. If β_n is too small, the convergence will be very slow. However, if it is too large, the algorithm will be unstable or divergent. To address this issue, the conjugate gradient method (Concus et al., 1976) is employed in this paper. The step size can be calculated by:

$$\beta_n = \frac{\left(\nabla^2 \mathrm{E}(\mathbf{p}_n)\mathbf{p}_n - \mathbf{Q}^{\mathbf{T}}\mathbf{Q}p'\right)^T \nabla \mathrm{E}(\mathbf{p}_n)}{(\nabla \mathrm{E}(\mathbf{p}_n))^T \left(\nabla^2 \mathrm{E}(\mathbf{p}_n)\right) \nabla \mathrm{E}(\mathbf{p}_n)} \tag{15}$$

where $\nabla^2 \mathrm{E}(\mathbf{p})$ is the Hessian matrix of the cost function $\mathrm{E}(\mathbf{p})$.

3. Experimental results

To test the performance of the proposed method, experiments were performed on both real and simulated ETM+ data. The data used were L1G products obtained from the USGS website (http://glovis.usgs.gov/). Considering the differences in spatial resolution, only bands 1–5 and band 7 were used in the experiments. All data used in the paper were cropped sub-images of 400×400 pixels, and were stored as the original 8-byte integer value.

Experiments were performed on both simulated images and real SLC-off images. The three multi-temporal data based methods of local linear histogram matching (LLHM) (Storey et al., 2005), neighborhood similar pixel interpolator (NSPI) (Chen et al., 2011), and the proposed WLR method were compared. Furthermore, the two non-reference methods of moving neighborhood kriging interpolation (MNKI) (Haas, 1990) and the proposed Laplacian prior regularization method (LPRM) were implemented for comparison purposes.

Table 1
The accuracy of the results recovered by local linear histogram matching (LLHM), neighborhood similar pixel interpolator (NSPI), and weighted linear regression (WLR), as shown in Fig. 2.

		LLHM	NSPI	WLR
r	B1	0.854	0.884	0.908
	B2	0.853	0.882	0. 912
	B3	0.833	0.868	0. 898
	B4	0.853	0.891	0. 915
	B5	0.861	0.911	0. 921
	B7	0.837	0.887	0. 904
ARE (%)	B1	2.974	2.464	2.258
	B2	4.231	3.601	3.200
	B3	7.183	6.094	5.473
	B4	11.043	7.992	7.136
	B5	14.891	9.461	8.979
	B7	17.506	12.207	11.178
UIQI	B1	0.852	0.884	0.908
	B2	0.850	0.882	0.913
	B3	0.829	0.868	0.898
	B4	0.849	0.890	0.915
	B5	0.854	0.911	0.923
	B7	0.833	0.887	0.904
MSA		4.456	3.178	2.861

3.1. Experiments on simulated SLC-off images

In the simulated experiments, the recovered images were compared with the original image by the calculation of several statistical indices, allowing a quantitative assessment. The first index used was the Pearson correlation coefficient (r). This metric can be used to assess

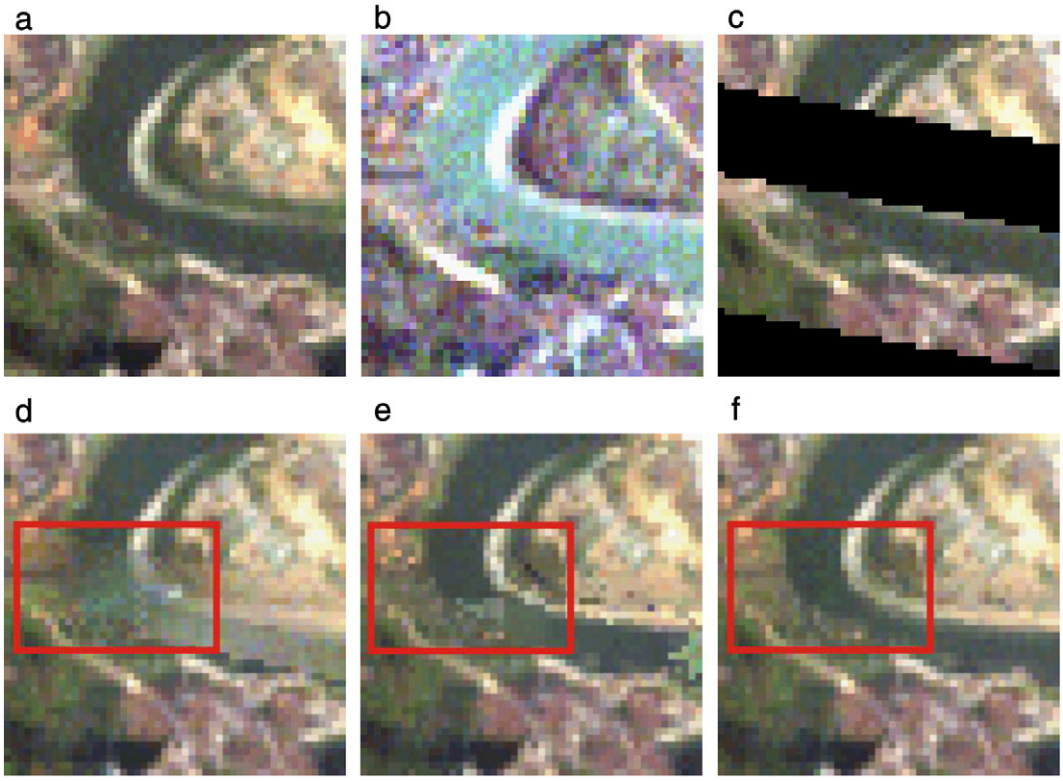

Fig. 3. (a)–(f) Detailed regions cropped from Fig. 2(a)–(f). (For interpretation of the references to color in this figure, the reader is referred to the web version of this article.)

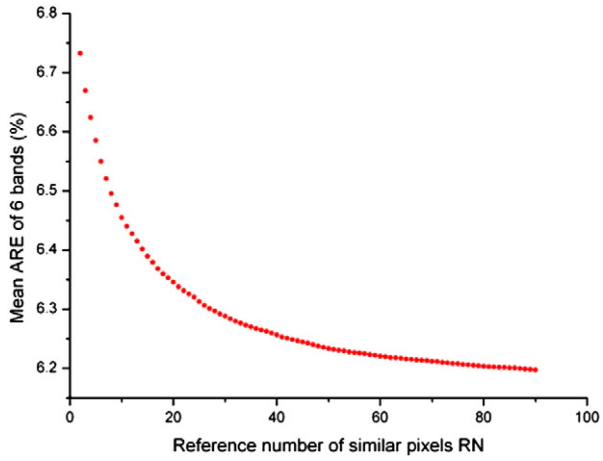

Fig. 4. The mean ARE of six bands when using different N_R values, as tested by Fig. 2(a)–(c).

the degree of consistency between predicted values and the observed values. It is defined as:

$$r = \frac{\sum_{j=1}^{M}\left(N_{Rj}-\overline{N}_R\right)\left(N_{Oj}-\overline{N}_O\right)}{\sqrt{\sum_{j=1}^{M}\left(N_{Rj}-\overline{N}_R\right)^2\sum_{j=1}^{M}\left(N_{Oj}-\overline{N}_O\right)^2}} \tag{16}$$

where M is the total number of gap pixels, and N_{Rj} and N_{Oj} are the recovered and original values of the jth invalid pixel, respectively. A larger r indicates a closer consistency between the two groups of pixels, and the data will be identical when r equals 1.0.

The second metric used was the average relative error (ARE) of a predicted value. It is defined as:

$$ARE = \left(\sum_{j=1}^{M}\left(\left|N_{Oj}-N_{Rj}\right|/N_{Oj}\right)\right)/M \times 100\%. \tag{17}$$

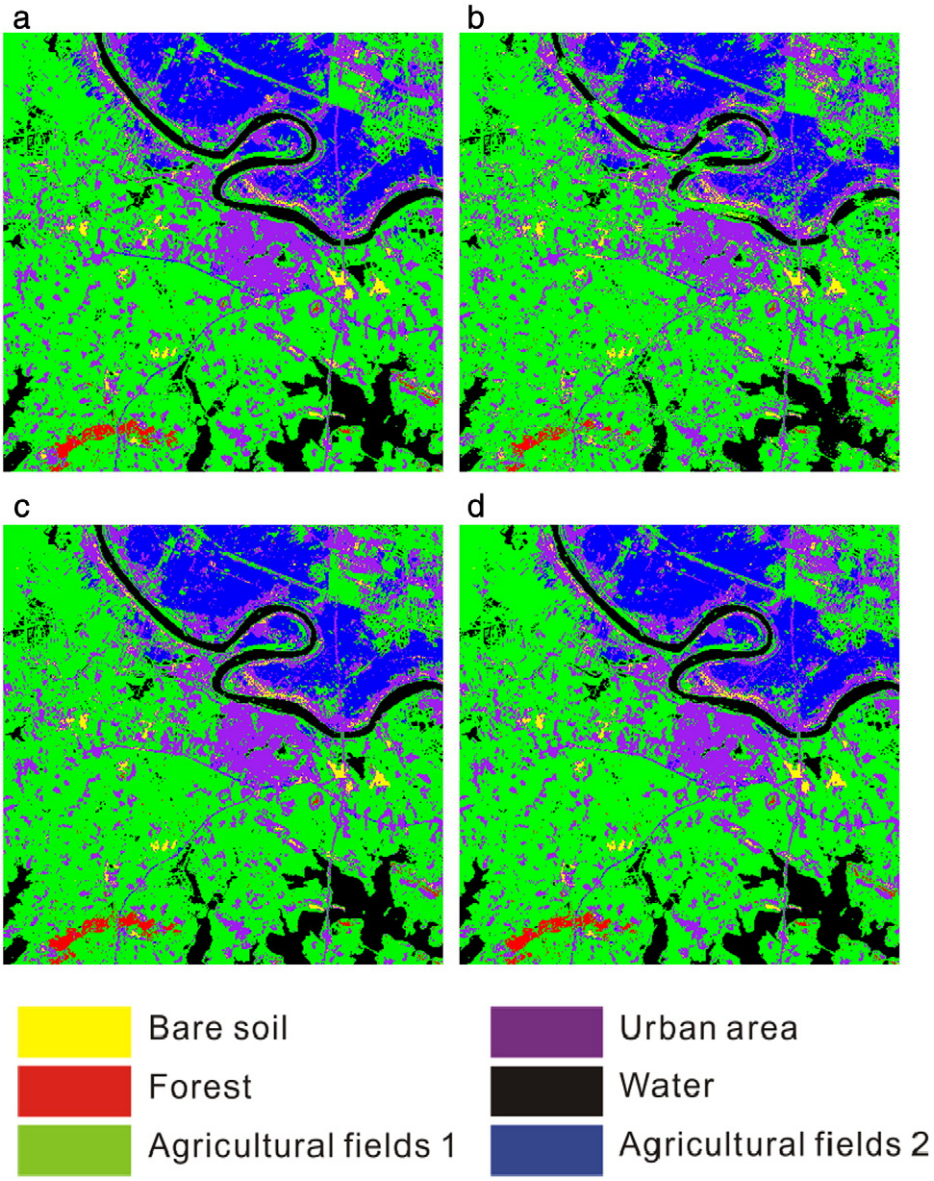

Fig. 5. The classification results corresponding to Fig. 2(a) and (d)–(f).

The smaller the ARE, the better the prediction.

A universal image quality index (UIQI) (Wang & Bovik, 2002) was also used. This indicator provides a measure of the closeness between the filled and the original areas by utilizing the differences in the statistical distributions.

$$UIQI = \frac{\sigma_{RO}}{\sigma_R \sigma_O} \cdot \frac{2\overline{N}_R \overline{N}_O}{\overline{N}_R{}^2 + \overline{N}_O{}^2} \cdot \frac{2\sigma_R \sigma_O}{\sigma_R{}^2 + \sigma_O{}^2} \tag{18}$$

where σ_{RO}, σ_R and σ_O are the covariance and the variances of the recovered and original regions, respectively. Under ideal conditions, UIQI equals 1.0.

As these three indices are calculated band by band, but the results can only display the effect on each single band. In order to assess the spectral fidelity, the mean spectral angle (MSA) was also employed. It can be calculated by (Dennison et al., 2004):

$$MSA = \left(\sum_{j=1}^{M} \arccos \left(\sum_{b=1}^{n} N_{Oj} N_{Rj} / \sqrt{\sum_{b=1}^{n} N_{Oj}{}^2 \sum_{b=1}^{n} N_{Rj}{}^2} \right) \right) / M \tag{19}$$

where n is the total number of bands. A smaller MSA value means that the prediction is better.

The first experiment region is located in Wuhan, China, around 30.59°N and 114.02°E, and is covered by Path 123 and Row 39 in World Reference System 2 (WRS-2). Fig. 2(a) and (b) shows the two tested ETM+ images (true color composite R = band 3, G = band 2, B = band 1), acquired on March 19, 2002, and December 29, 2001, respectively. The input primary image covered by the simulated gaps is shown in Fig. 2(c). In this experiment, the reference number of similar pixels (N_R) was set to 30, and the initial and maximum window sizes were 7 and 99, respectively.

Panels (d)–(f) of Fig. 2 are the output images recovered by the LLHM, NSPI and WLR methods, respectively. Generally, the image recovered by the proposed WLR method appears much closer to the actual image (Fig. 2(a)) than the other two methods. In Fig. 2(d), for LLHM, obvious artifacts can be found near the edge of the river. This result shows that when the image contains complex terrain, a simple linear algorithm using all the common pixels is unsatisfactory. In Fig. 2(e), for NSPI, most of the edges are well recovered, but there is noise in the recovered region. To facilitate a detailed visual inspection, zoomed regions cropped from Fig. 2(a)–(f) are shown in Fig. 3(a)–(f). The recovered details are emphasized with a red mark. Fig. 3(f), for WLR, shows the best visual result and is consistent with the original image. It is noteworthy that the two input images were acquired in different seasons, and the ground features have been significantly changed. The LLHM and NSPI methods cannot adapt to this change very well, so more errors occurred near the river's edges. Benefiting from the adapted similar-pixels searching procedure, the proposed WLR method was better able to address this issue.

In order to quantitatively compare the results of the above methods, the r, ARE, UIQI and MSA values of all the recovered pixels were compared. The results are listed in Table 1. Generally, WLR shows a higher accuracy in all the indices, compared with the other two methods.

As previously mentioned, the most important parameter that needs to be determined is the reference number of similar pixels, N_R, which also dominates the value of the initial and maximum window sizes. The determination of N_R was optimized through a series of comparative experiments, using the images shown in Fig. 2(a)–(c). The mean ARE values of the six bands were calculated using different N_R values from 2 to 90, and the result is shown in Fig. 4. It is apparent that the more pixels used in the reference, the more reliable the results. This is because of the advantage of the regression algorithm in that more sample points that make the estimation steadier. All the other metrics and filled results show similar results. However, considering that a larger N_R will greatly decrease the computational efficiency, and only improves the filling accuracy to an insignificant degree, we recommend 30 to 40 as an appropriate range of N_R. Moreover, in practical situations, the value of N_R can be adjusted, as appropriate, according to the demands of accuracy and computing time.

Table 2
The classification accuracies of the results recovered by local linear histogram matching (LLHM), neighborhood similar pixel interpolator (NSPI), and weighted linear regression (WLR), as shown in Fig. 2.

	LLHM	NSPI	WLR
OA	0.695	0.795	0.812
Kappa	0.484	0.664	0.693

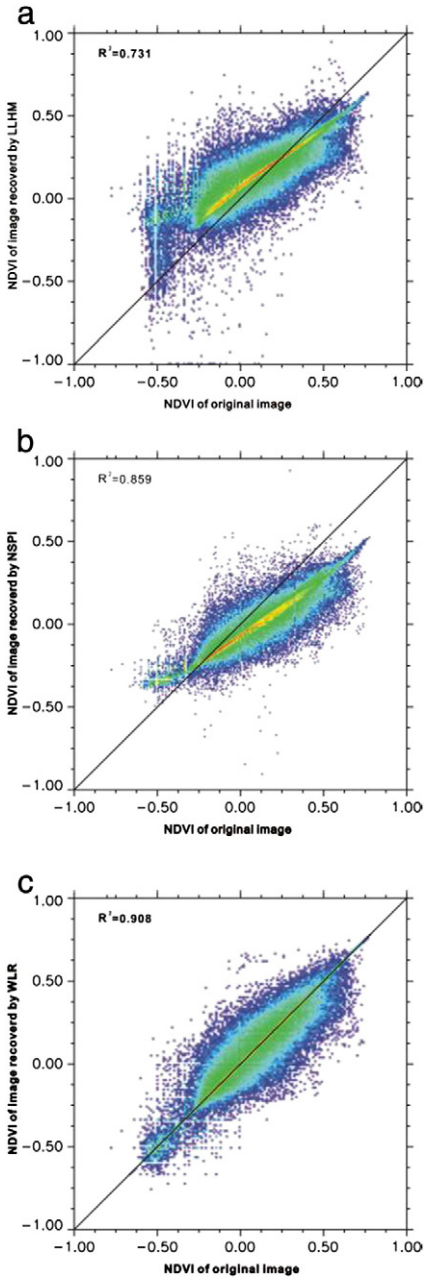

Fig. 6. The scatterplots of the real and the recovered NDVI values: (a) the LLHM method; (b) the NSPI method; and (c) the proposed WLR method. Yellow points represent a greater density of points, while blue points represent the opposite. (For interpretation of the references to color in this figure legend, the reader is referred to the web version of this article.)

In order to assess the capabilities of the recovered data for further applications, we produced land-cover images using the filled data shown in Fig. 2 and compared the results with an analogous classification generated from the original image data. Land-cover data were generated using the maximum likelihood supervised classifier, and high-resolution imagery from Google Earth was used to help define and categorize the sample points. The classification scheme consisted of the following land-cover categories: water, urban area, agricultural fields, forest and bare soil. The sample areas were selected from the valid region of the original image. The classification results shown in Fig. 5(a)–(d) correspond to the images of Fig. 2(a) and (d)–(f). Table 2 shows the accuracy assessment of the classifications of all the filled pixels, using the classification map of the original image as reference data. For WLR, relatively high values of OA (overall accuracy) and kappa (Congalton & Green, 2008) indicate a strong agreement between the classifications of the recovered image and the actual image. The classification of the LLHM result has the lowest values of OA and kappa, and the NSPI result shows an intermediate level of accuracy.

In addition, to further assess the usability of the recovered data in quantitative applications, the normalized difference vegetation indices (NDVI) of the filled images were also compared. An atmospheric correction of a dark object subtraction method (Chavez, 1988) was implemented before the NDVI calculation. According to the scatterplots shown in Fig. 6, it is apparent that LLHM estimated the values of the un-scanned locations with larger errors, the results derived from NSPI have a better agreement with the reference data, but the proposed method still gave the best performance. The R^2 value of the LLHM result is 0.731, which is the lowest, and the NSPI result is 0.859, which shows an obvious increase. The result of the proposed WLR method gives the highest value of 0.908. It should be noted that the outliers in the recovered images can significantly affect the atmospheric correction procedure, and that is the reason why there are biases in the former two

Table 3
The accuracies of the results recovered by moving neighborhood kriging interpolation (MNKI) and the Laplacian prior regularization method (LPRM), as shown in Fig. 7.

		MNKI	LPRM
r	B1	0.904	0.926
	B2	0.960	0.972
	B3	0.977	0.985
	B4	0.981	0.989
	B5	0.976	0.984
	B7	0.977	0.984
ARE (%)	B1	4.050	3.633
	B2	4.908	4.119
	B3	6.270	5.392
	B4	7.053	5.390
	B5	10.420	8.708
	B7	10.589	9.412
UIQI	B1	0.903	0.926
	B2	0.960	0.972
	B3	0.977	0.985
	B4	0.981	0.989
	B5	0.976	0.984
	B7	0.977	0.983
MSA		2.354	2.246

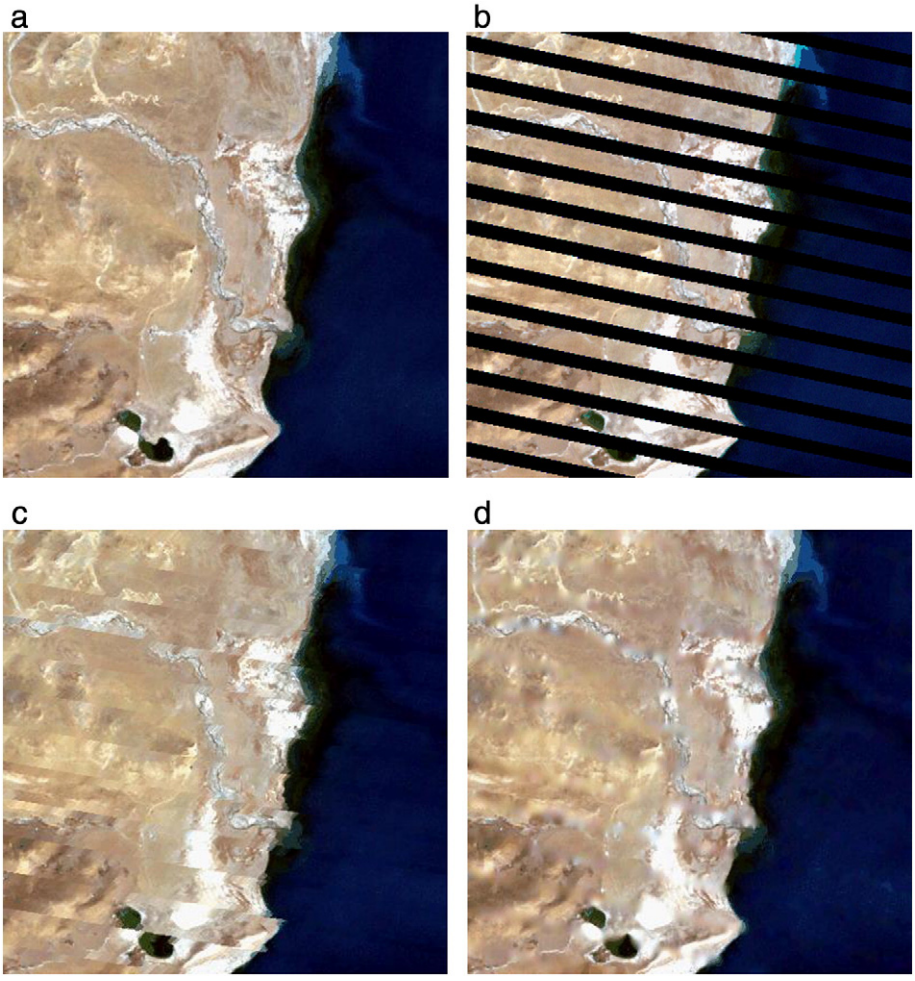

Fig. 7. Landsat SLC-on ETM + images for the simulated experiment: (a) original SLC-on image; (b) SLC-off image simulated by (a); (c) and (d) are the results recovered by MNKI and LPRM, respectively.

plots. In summary, due to its robustness, the proposed method can be widely applied. These results demonstrate that the gap-filled results derived from the new method can provide a better support for applications such as land-cover mapping and NDVI calculation.

In the previous experiment, the proposed multi-temporal recovery method was tested. The following experiment was implemented for the validation of the non-reference method. The 400 × 400 pixels Landsat area is located in Tibet, around 30.72°N and 90.25°E. The original image of the experiment region is shown in Fig. 7(a), and the corresponding simulated gap image is shown in Fig. 7(b). The recovered images using MNKI and LPRM are shown in Fig. 7(c) and (d), respectively. In Fig. 7(c) of MNKI, obvious artifacts can be seen at the junction of water and land. On the one hand, MNKI cannot adequately fit the scene changes, and, on the other hand, the gap width is beyond the filling capabilities of the algorithm. Therefore, the artifact phenomenon is particularly significant. In Fig. 7(d), LPRM provides a better visual connectivity, and this is further supported by the quantitative accuracy assessment shown in Table 3.

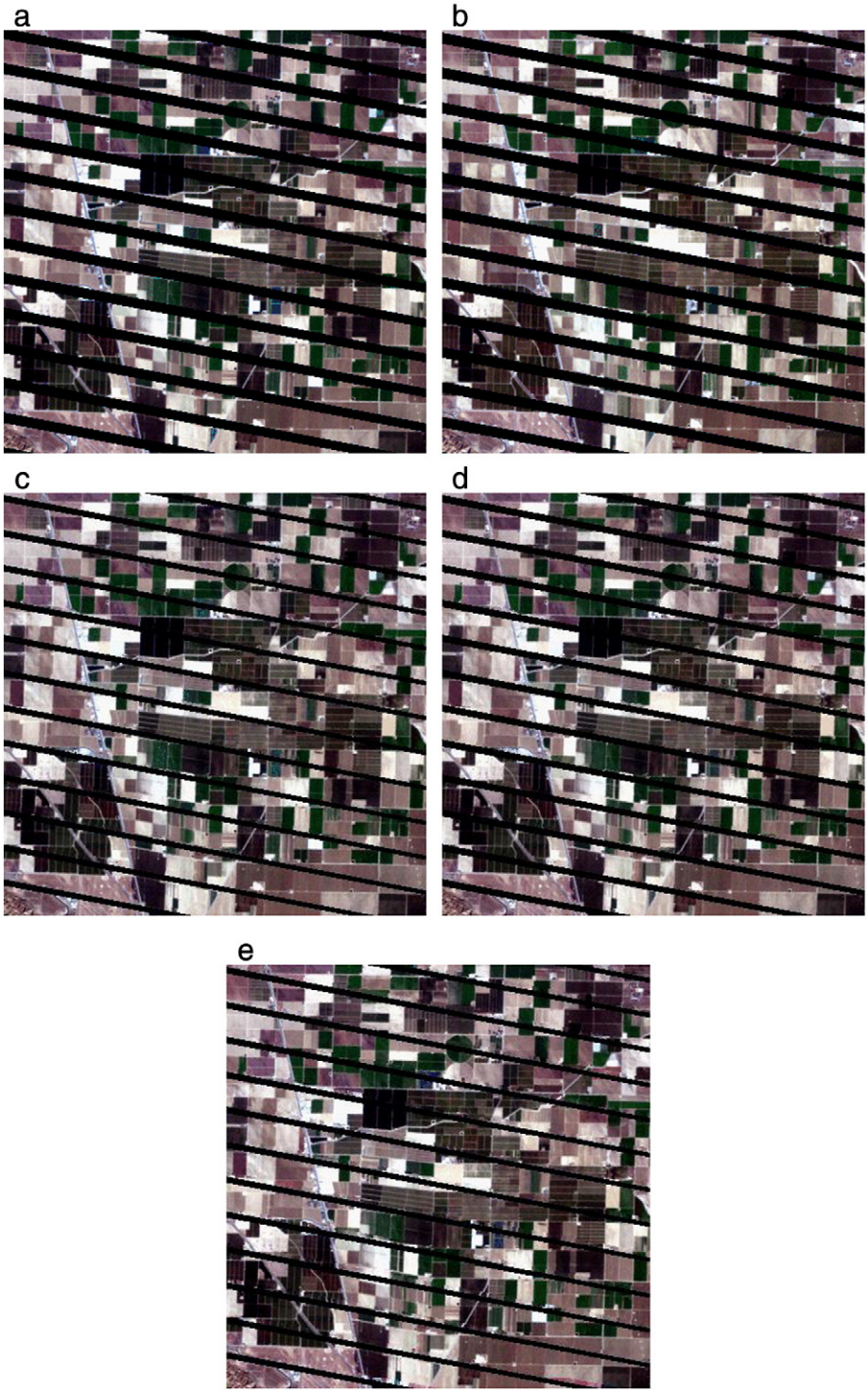

Fig. 8. Landsat SLC-off ETM+ images: (a)–(b) acquired on October 23, 2011, and November 8, 2011, respectively; (c)–(e) are the results recovered by LLHM, NSPI and WLR, respectively.

3.2. Experiments using actual SLC-off images

To further verify the efficacy of the proposed method, experiments using actual SLC-off images were implemented. The first experimental region of real data is located in California, U.S., around 39.10°N and 76.14°W, and is covered by WRS 2 Path 41 and Row 36. Regular features formed by vegetation and bare soil are distributed over the area.

Fig. 8(a) and (b) shows the two tested SLC-off ETM+ images acquired on October 23, 2011, and November 8, 2011, respectively. Panels (c)–(e) of Fig. 8 are the results recovered by the LLHM, NSPI and WLR methods, respectively. As the gaps cannot be completely covered by the single auxiliary SLC-off image, there are still invalid pixels remaining in the recovered images. The zoomed regions cropped from Fig. 8(c)–(e) are shown in Fig. 9(a)–(c). The recovered details are also marked. As the two input images are temporally close, no significant changes occurred, and the ground features are very regular, the three recovered results are relatively close to each other. In Fig. 9(a), as with the results of the simulated experiments, there are obvious artifacts near the edges of the ground features. In Fig. 9(b), noise can still be found in the edge regions. As can be seen in Fig. 9(c), the proposed algorithm achieved the best visual effects. It is worth noting that the remaining gaps in Fig. 8(d) are wider than for the other two methods. This is because, in the NSPI method, only the pixels that have valid values in all bands can be used to fill the gap pixels. As the gaps are not completely covered in each band, the pixels near the gaps do not have valid values in all bands. Therefore, some referable information is omitted in the NSPI method. In this respect, the proposed method can better use all the auxiliary information.

The remaining gaps in Fig. 8(c) were filled by MNKI and LPRM, respectively, and the results are shown in Fig. 10. In Fig. 10(c), the edge of the circular object is incorrectly filled. However, the sharpness is much better preserved in the filled image of Fig. 10(d). This demonstrates that the shape of a ground feature can be better recovered by the use of the proposed regularization method.

The second experiment region is located in eastern Maryland, U.S., around 39.10°N and 76.14°W, and is covered by Path 15 and Row 33. The primary image was acquired on February 11, 2008. Another image acquired on June 2, 2008 was used as the fill image. Almost all the missing pixels can be recovered by just employing WLR. The recovered image is shown in Fig. 11. Four sub-images chosen from the verge area and the corresponding original images are zoomed. This experiment demonstrates that the proposed method can be used in the production of entire Landsat scenes. The satisfactory details also verify that the algorithm is applicable to different scene types.

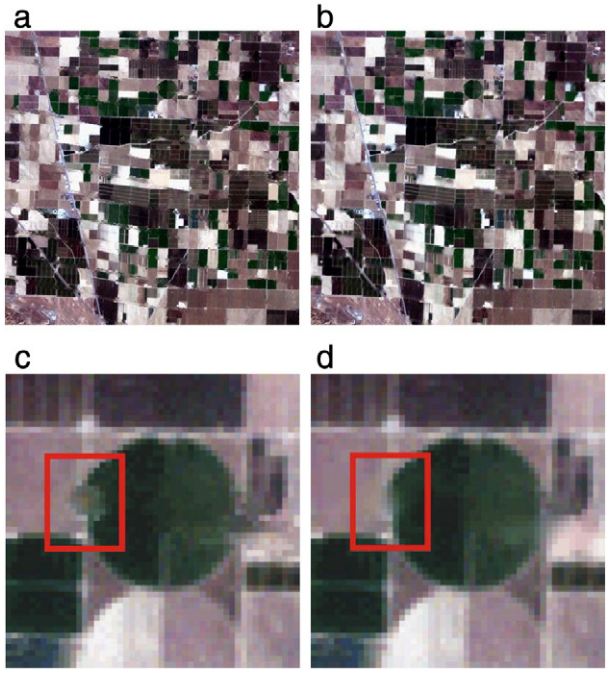

Fig. 10. Landsat SLC-off ETM+ images: (a) and (b) are the results using Fig. 8(e) recovered by MNKI and LPRM, respectively; (c) and (d) are detailed regions cropped from (a) and (b).

4. Discussion and conclusion

Despite the malfunction of the SLC, the quality of the radiometry and geometry of the Landsat 7 ETM+ data is still excellent for many applications. Therefore, in order to make better use of this important data source, it is necessary to develop techniques to recover the missing information in the SLC-off imagery. Considering the limitations of the existing restoration methods, this paper proposes an integrated method to fill the un-scanned gaps. With multi-temporal auxiliary data, the proposed WLR method can restore the invalid pixels accurately, even when obvious changes take place. Furthermore, in the case of lacking enough auxiliary information, the regularization recovery method can completely fill the remaining gaps by using the spatial information of the whole image. For the regions with undesirable climate condition which causes frequent cloud cover, this characteristic is especially important.

The proposed method can make good use of the consistency in object changes. Beforehand, according to the scatterplot study of ETM+ images, the hypothesis that pixels in unchanged or regularly changed regions share a linear correlation with similar pixels is proposed. This is the foundation of the following recovery method using multi-temporal images. Subsequently, an adapted similar-pixel searching method is proposed. The procedure can determine an appropriate threshold for each pixel in each band. Using this adapted threshold, the similar pixels can be accurately selected in various scene types. This is partly why the proposed method is more effective in complex scene types. In addition,

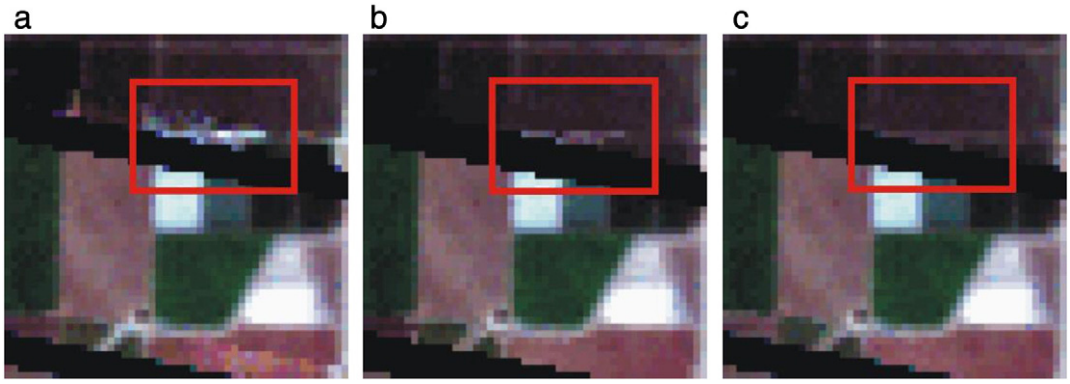

Fig. 9. (a)–(c) Detailed regions cropped from Fig. 8(c)–(e).

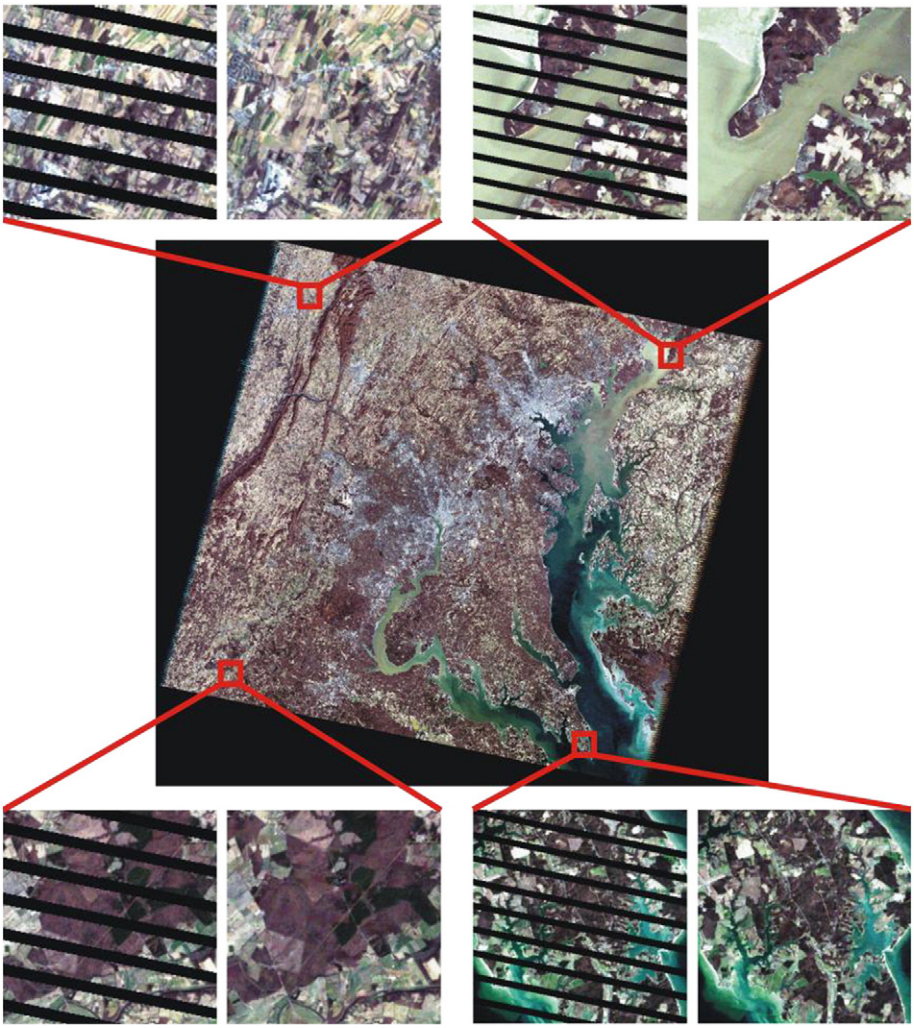

Fig. 11. An entire recovered Landsat SLC-off ETM+ image with the detailed regions and the corresponding original sub-images.

a reference number of similar pixels (N_R) is suggested in this procedure. After that, the WLR method using similar pixels is implemented. With an appropriate number of concerned pixels, the result of the linear regression algorithm can be more reliable. It is worth noting that the WLR method is based on the precondition that the ground features change regularly between scenes. The recovered result may be unsatisfactory when the scenes change abruptly.

Furthermore, to cope with the situation where not all of the gap pixels can be covered by valid multi-temporal auxiliary data, a non-reference filling method is proposed. By considering the spatial correlation of the observed scene, a simple regularization method using a Laplacian prior is employed to restore the remaining gaps. This approach does not require the availability of timely and cloud-free ETM+ images, and is requisite for regions with a changeable climate, such as humid tropical forest areas. However, this method cannot restore complicated textures when the invalid area is too large.

It should be noted that there are also several potential limitations for the proposed method. Only local spectrally similar pixels are used in the regression algorithm. However, it is worth noting that non-local information (Gilboa & Osher, 2008), which contains the structures and textures of the regions far from the missing pixel, can also play an important role in the recovery procedure. Several studies (Lou et al., 2010; Peyré et al., 2008) have shown that using the constraint of a non-local regularization method can effectively improve the detailed texture of the processing results. We will explore how such non-local information affects the recovery result in our future work.

There are some predetermined parameters for the proposed method. As an adaptive threshold determination approach is used in the WLR method, only the window size and N_R are critical for the result. As for LPRM, the determination of the regularization parameter λ is the most important part. However, these parameters are not sensitive to the different scenes. Therefore, for most regions, satisfactory products can be generated by using a set of fixed parameters.

It should also be noted that the main disadvantage of the proposed method is its relatively slow computing speed. In the experiments, it took about five times the time of LLHM to fill the gaps. However, considering the high accuracy, the relatively slow computing speed is acceptable. Furthermore, the computing time can be markedly reduced by shrinking the maximum searching window size, with the cost of a slight precision loss. As every pixel is filled independently and uses local information only, a parallel processing scheme based on a graphics processing unit (GPU) can be used in the bulk processing. Additionally, the computing efficiency can be further improved by using a hybrid tactic. The advantage of the WLR method is the relatively high accuracy in complex regions. For homogeneous regions, the LLHM method can still yield acceptable results. Therefore, these two methods can be hybridized and automatically switched according to the situation.

It is unclear how the spatial difference affects the recovery result (Brunsdon, 1998). When we tried to combine the spectral difference and the spatial difference, the experimental results demonstrated that the spatial difference has a greater impact on the recovery result than the spectral difference. We therefore used the squared Euclidean

distance in Eq. (4) when computing the integrated weight. In our future research, more spatial weighting functions will be tested and calibrated.

Acknowledgments

This work was supported in part by the Major State Basic Research Development Program of China (973 Program) under Grants 2009CB723905 and 2011CB707103, the National Natural Science Foundation of China under Grants 40930532, 40971220 and 41271376 and the Fundamental Research Funds for the Central Universities under Grant 2012619020210. We also thank the anonymous reviewers for their constructive comments.

References

Arvidson, T., Goward, S., Gasch, J., & Williams, D. (2006). Landsat-7 long-term acquisition plan: Development and validation. *Photogrammetric Engineering and Remote Sensing*, *72*, 1137–1146.

Boloorani, A. D., Erasmi, S., & Kappas, M. (2008a). Multi-source remotely sensed data combination: Projection transformation gap-fill procedure. *Sensors*, *8*, 4429–4440.

Boloorani, A. D., Erasmi, S., & Kappas, M. (2008b). Multi-source image reconstruction: Exploitation of EO-1/ALI in Landsat-7/ETM+ SLC-off gap filling. *Proceedings of image processing: Algorithms and systems VI* (pp. 681219). (San Jose, California).

Brunsdon, C. (1998). Geographically weighted regression: A natural evolution of the expansion method for spatial data analysis. *Environment and planning A*, *30*, 1905–1927.

Chavez, P. S. (1988). An improved dark-object subtraction technique for atmospheric scattering correction of multispectral data. *Remote Sensing of Environment*, *24*, 459–479.

Chen, F., Tang, L., & Qiu, Q. (June 18–20). Exploitation of CBERS-02B as auxiliary data in recovering the Landsat7 ETM+ SLC-off image. *Proceedings of the 18th International Conference on GeoInformatics* (Beijing, China).

Chen, J., Zhu, X., Vogelmann, J. E., Gao, F., & Jin, S. (2011). A simple and effective method for filling gaps in Landsat ETM+ SLC-off images. *Remote Sensing of Environment*, *115*, 1053–1064.

Concus, P., Golub, G. H., & O'Leary, D. P. (1976). *A generalized conjugate gradient method for the numerical: Solution of elliptic partial differential equations: Computer Science Department, School of Humanities and Sciences.* : Stanford University.

Congalton, R. G., & Green, K. (2008). *Assessing the accuracy of remotely sensed data: Principles and practices* (2nd ed.). Boca Raton: CRC Press.

Dennison, P. E., Halligan, K. Q., & Roberts, D. A. (2004). A comparison of error metrics and constraints for multiple endmember spectral mixture analysis and spectral angle mapper. *Remote Sensing of Environment*, *93*, 359–367.

Gilboa, G., & Osher, S. (2008). Nonlocal operators with applications to image processing. *Multiscale Modeling and Simulation*, *7*, 1005–1028.

Haas, T. C. (1990). Kriging and automated variogram modeling within a moving window. *Atmospheric Environment. Part A. General Topics*, *24*, 1759–1769.

Ju, J., & Roy, D. P. (2008). The availability of cloud-free Landsat ETM+ data over the conterminous United States and globally. *Remote Sensing of Environment*, *112*, 1196–1211.

Lauer, D. T., Morain, S. A., & Salomonson, V. V. (1997). The Landsat program: Its origins, evolution, and impacts. *Photogrammetric Engineering and Remote Sensing*, *63*, 831–838.

Lee, D. S., Storey, J. C., Choate, M. J., & Hayes, R. W. (2004). Four years of Landsat-7 on-orbit geometric calibration and performance. *IEEE Transactions on Geoscience and Remote Sensing*, *42*, 2786–2795.

Lou, Y., Zhang, X., Osher, S., & Bertozzi, A. (2010). Image recovery via nonlocal operators. *Journal of Scientific Computing*, *42*, 185–197.

Markham, B. L., Arvidson, T. J., Goward, S. N., Barsi, J., & Scaramuzza, P. (2006). Landsat-7 long-term acquisition plan radiometry: Evolution over time. *Photogrammetric Engineering and Remote Sensing*, *72*, 1129.

Maxwell, S., Schmidt, G., & Storey, J. (2007). A multi-scale segmentation approach to filling gaps in Landsat ETM+ SLC-off images. *International Journal of Remote Sensing*, *28*, 5339–5356.

Peyré, G., Bougleux, S., & Cohen, L. (2008). Non-local regularization of inverse problems. *ECCV'08: European Conference on Computer Vision* (pp. 57–68). Berlin: Springer.

Pringle, M. J., Schmidt, M., & Muir, J. S. (2009). Geostatistical interpolation of SLC-off Landsat ETM+ images. *ISPRS Journal of Photogrammetry and Remote Sensing*, *64*, 654–664.

Reza, M. M., & Ali, S. N. (2008). Using IRS products to recover 7ETM+ defective images. *American Journal of Applied Sciences*, *5*, 618–625.

Roy, D. P., Ju, J., Lewis, P., Schaaf, C., Gao, F., Hansen, M., et al. (2008). Multi-temporal MODIS-Landsat data fusion for relative radiometric normalization, gap filling, and prediction of Landsat data. *Remote Sensing of Environment*, *112*, 3112–3130.

Ruppert, D., & Wand, M. P. (1994). Multivariate locally weighted least squares regression. *The Annals of Statistics*, 1346–1370.

Shen, H., Liu, Y., Ai, T., Wang, Y., & Wu, B. (2010). Universal reconstruction method for radiometric quality improvement of remote sensing images. *International Journal of Applied Earth Observation and Geoinformation*, *12*, 278–286.

Shen, H. F., & Zhang, L. P. (2009). A MAP-based algorithm for destriping and inpainting of remotely sensed images. *IEEE Transactions on Geoscience and Remote Sensing*, *47*, 1490–1500.

Storey, J., Scaramuzza, P., Schmidt, G., & Barsi, J. (October 23–27). Landsat 7 scan line corrector-off gap-filled product development. *Proceedings of Pecora 16 Global Priorities in Land Remote Sensing*. South Dakota: Sioux Falls.

Strong, D., & Chan, T. (2003). Edge-preserving and scale-dependent properties of total variation regularization. *Inverse problems*, *19*, S165.

USGS (2003). Preliminary assessment of the value of Landsat 7 ETM+ data following scan line corrector malfunction. Available online at http://landsat.usgs.gov/documents/SLC_off_Scientific_Usability.pdf (accessed 8 May 2010).

Van der Meer, F. (2012). Remote-sensing image analysis and geostatistics. *International Journal of Remote Sensing*, *33*, 5644–5676.

Wang, Z., & Bovik, A. C. (2002). A universal image quality index. *IEEE Signal Processing Letters*, *9*, 81–84.

Woodcock, C. E., Allen, R., Anderson, M., Belward, A., Bindschadler, R., Cohen, W., et al. (2008). Free access to Landsat imagery. *Science*, *320*, 1011.

Wulder, M. A., White, J. C., Masek, J. G., Dwyer, J., & Roy, D. P. (2011). Continuity of Landsat observations: Short term considerations. *Remote Sensing of Environment*, *115*, 747–751.

Yuan, Q., Zhang, L., & Shen, H. (2012). Multi-frame super-resolution employing a spatially weighted total variation model. *IEEE Transactions on Circuits And Systems For Video Technology*, *22*, 379–392.

Zhang, C., Li, W., & Travis, D. (2007). Gaps-fill of SLC-off Landsat ETM+ satellite image using a geostatistical approach. *International Journal of Remote Sensing*, *28*, 5103–5122.

Zhang, L., Yuan, Q., Shen, H., & Li, P. (2011). Multiframe image super-resolution adapted with local spatial information. *Journal of the Optical Society of America. A*, *28*, 381–390.